Statistical Investigation of the Storm Time Plasma Density Strip-like Bulges at Lower-Mid Latitudes

Wenyu Du[1,2], Jiahao Zhong[1,2], Xin Wan[1,2], Yongqiang Hao[1], Chao Xiong[3], Hui Wang[3], Jun Cui[1], Yiwen Liu [4], Qiaoling Li[5], Jiawei Kuai[6]

[1]Planetary Environmental and Astrobiological Research Laboratory (PEARL), School of Atmospheric Sciences, Sun Yat-sen University, Zhuhai, China.

[2]Key Laboratory of Tropical Atmosphere-Ocean System, Ministry of Education, Zhuhai, China

[3]Department of Space Physics, College of Electronic Information, Luojia Laboratory, Wuhan University, 430079 Wuhan, China.

[4]School of Physics and Electronic Information, Shangrao Normal University, Shangrao, China.

[5]School of Petroleum, China University of Petroleum-Beijing at Karamay, Xinjiang, China

[6]College of Astronautics, Nanjing University of Aeronautics and Astronautics, Nanjing, China

Corresponding Author: Xin Wan (wanx7@mail.sysu.edu.cn)

Key points:

1. Occurrence of bulge has no strict limitation but shows some dependences on longitude, storm intensity, local time, and solar activity
2. Midlatitude extra density peak could be recognized as a precursor of the strip-like bulge
3. Ion drift within the flux tube of the bulges is mainly in the field-aligned downward/cross-L inward pattern

Abstract

The strip-like bulge is a storm-time conjugate ionospheric plasma density enhancement that extends widely (over 150° in longitude) in the zonal dimension but occupies only 1°~5° in latitude. Based on in-situ measurements of 11 low earth orbit (LEO) satellites, this study statistically investigates the bulge structures of geomagnetic storms driven by 136 interplanetary coronal mass ejections (ICMEs) during 2000~2021. The statistical results show that the strip-like bulges are initiated at the end of the storm main phase and can persist for more than 60 hours. The spatial and temporal coverage of the strip-like bulge varies from storm to storm. However, the bulges do exhibit occurrence preferences: stronger storms, the Asian-Pacific sector (with eastward magnetic declination), the nightside of the dawn-dusk terminator, and solar minimum periods. A quiet time density enhancement called midlatitude extra peaks could be recognized as a precursor of the strip-like bulge. The plasmaspheric compression shares some similar occurrence features with the strip-like bulge, indicating a field-aligned downward and cross-L inward intrusion of the plasmaspheric ions. The local net ion drifts partly support this scenario with downward/inward being the most dominant but not unique pattern, other diverse net ion drift configurations exist but their impact on the strip-like bulges remains unclear.

Plain Language Summary

A geomagnetic storm is a major disturbance of Earth's magnetic field when energy from the solar wind is effectively injected into the space environment surrounding Earth. During a storm, the ionosphere from 80 to 1000 km is affected, and a sharp increase in ionospheric ion density with a narrow latitudinal range could be observed at low-mid latitudes. The main ions constituting the sharp increase are H^+/He^+, which are the primary ions in the plasmasphere. We called this increase the ‘bulge’. Towards a better understanding of the principle nature as well as the formation mechanisms of the structure, we extracted a number of samples snapshotted by many satellites to conduct a statistical investigation. It is found that the bulges prefer to appear in the Asian-Pacific region, at 18:00-06:00 LT, during strong storms, and under solar minimum conditions. Before their appearance, a smoother density peak structure is often observed, which could be recognized as the precursor. We suggested a substantial transfer of ions from higher to lower altitudes, causing the smoother density peak structure to evolve into the bulge.

1 Introduction

Recently, an intriguing type of ionospheric irregularity, namely, strip-like plasma density bulge (Wan et al., 2021; Wan et al., 2022), has been found to occur at low-to-middle latitudes during periods of geomagnetic disturbance. The structure appears conjugately in both the northern and southern hemispheres as a narrow strip, with a longitudinal extent of up to 150° and a latitudinal extent of approximately 5°. It appears from the storm main phase and persistently survives through the recovery phase for about two days, covering all the local time sectors.

This strip-like plasma density bulge has been observed for several years. However, previous investigations have not been aware of its extremely wide zonal extension, and have treated it as a rather localized phenomenon. The nomenclature of this structure differs from each other in different investigations. Tsurutani et al. (2004) and Mannucci et al. (2005) noted the structure from satellite observations and named it the shoulder. Other terminologies, such as the streak of high plasma density (Park et al., 2012), nighttime ionospheric localized enhancements (NILE) (Datta-Barua et al., 2008; Foster & Rideout, 2007) or storm-induced plasma streams (SIPS) (Maruyama et al., 2013), have been proposed for the bulge structure based on various types of observations. Reports of the bulges are relatively rare compared to those of many other well-known storm-time ionospheric phenomena, implying that the bulges may not regularly appear during all geomagnetic storm events. As will be presented in this study, the bulge can be frequently absent, which raises the question of what is the determining factor to control the appearance of the strip-like bulge for a given geomagnetic storm.

Another issue concerns the spatial and temporal characteristics of the bulge. During the 7 September 2017 storm event, a strip-like bulge was found at 120°~270° E longitude, which occupies the areas with eastward magnetic declinations (Wan et al., 2021). Whereas the coverage changed to 150°~330° E, but still includes the eastward magnetic declination area, for the 4 November 2021 storm case (Wan et al., 2022). Other historical observations have shown the bulges in various places, including the East Asia sector (Maruyama et al., 2013) and the West Pacific and American sectors (Chartier et al., 2021; Datta-Barua et al., 2008; Foster & Rideout, 2007). The above results also showed that the observed bulges could appear at all local times, and mainly initiated at the storm main phase and persisted through the recovery phases. However, why the longitudinal coverage changes for different storm cases is unknown, and local time dependence had not been statistically investigated.

Early studies revealed that the bulge usually occurred during severe geomagnetic storms and was associated with the appearance of a significantly enhanced/expanded equatorial ionization anomaly (EIA) (Chartier et al., 2021; Mannucci et al., 2005; Tsurutani et al., 2004). However, recent work (Wan et al., 2022) has shown that this narrow (in meridional dimension) strip-like structure might evolve from a local vast density enhancement at midlatitudes (with a meridional extension over 15° in latitude) rather than EIA. This vast enhancement, namely the middle-latitudinal band structures or midlatitude extra peaks, had previously been observed mainly during the night (Cai et al., 2022; Li et al., 2018; Wan et al., 2021; Xiong et al., 2019; Zhong et al., 2019), but could also be occasionally captured during daytime (Kuai et al., 2021; Rajesh et al., 2016). Whether the peak structures are necessary for the formation of the bulges is ambiguous. Wan et al. (2022) observed that when a vast density enhancement structure was transformed into a strip-like bulge, the direction of ion drift changed. Whether the peak structure is a precursor of bulges, and the main driving mechanism for the transformation from the precursor to bulge needs further study.

Regarding the specific formation and evolution process of bulges, previous studies suggest that it may be related to the compression of the plasmasphere (Horvath & Lovell, 2008; Obana et al., 2019; Tsurutani et al., 2004; Wan et al., 2021). Compression of the plasmasphere leads to the earthward movement of plasma during the main phase and contributes to the formation of bulges (Horvath & Lovell, 2008; Tsurutani et al., 2004). The plasmaspheric intrusion into the ionosphere, in the form of either the field-aligned downward filling or cross-L inward compression, might explain that the bulges are purely constituted by the H^+/ He^+ rather than the ionospheric O^+. The ion drift can effectively characterize the plasma transport during the formation and development of bulges, but the ion drift from several DMSP orbits with bulge signatures revealed no downward ion drift configuration (Wan et al., 2021). Along with the initiation of the strip-like bulge, the equatorward turning of the neutral wind was observed by Ionospheric Connection Explorer (ICON), followed by a similar turning of the plasma drift from downward to upward field-aligned flux (Wan et al., 2022), which strongly indicates the driving forces generated from storm-induced disturbed neutral winds. However, the ion drift configuration under the combined effects of the plasmaspheric compression and disturbed neutral winds is still not understood, and the effect of the induced plasma transport on the formation of bulges is also not clear.

To address the aforementioned issues, this paper conducts a statistical analysis of bulge samples. In the following, Section 2 introduces the data and methods. Section 3 describes the statistical properties of all the selected storm events. Section 4 presents the detailed spatial and temporal characteristics of the strip-like bulge. Section 5 discusses the possibility of broader midlatitude extra peaks as precursors to the latitudinally narrow bulges. Section 6 proposes a possible formation mechanism for bulges in conjunction with the plasmaspheric composition, and the conclusion is given in Section 7.

2 Data and Methods

The spatial and temporal coverage of the observations should be rich enough for a statistical purpose that requires as many bulge events as possible. In the spatial dimension, we adopt the data from 11 high-inclination LEO satellites to ensure good longitudinal and local time coverage. A detailed illustration is provided below. In the temporal dimension, we revisited 136 storm events during the last 21 years (2000-2021).

2.1 In Situ Observations from LEO Satellites

The in-situ data measured by 11 LEO satellites collected over 20 years were used in this study, including DMSP, CHAMP, GRACE, and Swarm data.

The Defense Meteorological Satellite Program (DMSP) series satellites operate in a sun-synchronous polar orbit at approximately 840 km. Each satellite is equipped with a Special Sensor for Ions, Electrons, and Scintillation (SSIES), which is capable of measuring the ion density at the orbital position of the satellite. Additionally, through Retarding Potential Analyzer (RPA) sweep analyses, the O^+ density and H^+/ He^+ density can be derived. This study utilized data from DMSP F12, F13, F14, F15, F16, F17 and F18 from 2000 to 2021.

Swarm is a constellation that comprises three satellites: Swarm Alpha (A), Bravo (B), and Charlie (C). The onboard Langmuir probes provide ion density (*Ni*) measurements with a 2 Hz sampling rate. Swarm A and C flew side by side at approximately 470 km with a longitudinal separation of approximately 1.4°, which made their electron density measurements similar, while Swarm B flew alone at approximately 520 km. Therefore, we adopted the data from Swarm A and Swarm B.

The CHAMP (Challenging Mini-satellite Payload) satellite was launched on 15 July 2000 into a circular, near-polar (87.3° inclination) orbit with an initial altitude of approximately 450 km, which decayed to 330 km in 2009. The Planar Langmuir Probe (PLP) sampled the in-situ electron density at a time of 15 s.

The GRACE (Gravity Recovery and Climate Experiment) satellites, which comprise two spacecraft, GRACE-A and GRACE-B, were launched on 17 March 2002 into a near-circular, polar orbit (89° inclination) with an initial altitude of approximately 490 km. The horizontal separation of the two satellites is approximately 200 km. The total electron content between the spacecraft can be deduced through the measurements of the dual one-way range change between both satellites by the onboard K-Band Ranging System (KBR) system. The averaged electron density can be further obtained by dividing the horizontal TEC by the distance between the spacecraft (Xiong et al., 2019).

Figures 1a and 1b show the LTs information during the equator crossing that belongs to one of the semi-orbits; the LTs of the other half orbits should be added by 12 hours. The high inclination made in-situ observations of the satellite more or less in the meridional direction, with two concentrated local times (LTs) corresponding to the ascending and descending orbits. The local times of sun-synchronous DMSP satellites are more stable than those of other satellites but exhibit long-term shifts (in years). The polar orbit satellites (Swarm, CHAMP, GRACE) travel all the local time for approximately 140 days. Therefore, during the investigation period (2000-2021), the observations cover all the local times but include denser data from the dawn-dusk sector, mainly from DMSP satellites.

2.2 Geomagnetic Storm Events

A total number of 136 geomagnetic storm events were used in this study; these events were interplanetary coronal mass ejections (ICMEs) driven type, which were selected from the list of near-Earth ICMEs summarized by Richardson and Cane (2010) (https://izw1.caltech.edu/ACE/ASC/DATA/level3/icmetable2.htm). The geomagnetic storm in the previous bulge investigation had relatively strong intensities. For example, the Dst index during the 5–6 November 2001 storm (Tsurutani et al., 2004) and the 29–30 October 2003 storm (Mannucci et al., 2005) reached minimum values of -275 nT and -350 nT, respectively, whereas two recent studies acquired geomagnetic storms have minimum SYM-H index below -100 nT (Wan et al., 2021; Wan et al., 2022). Therefore, the selection of storm events requires only one condition: the minimum SYM-H index should be less than -50 nT to ensure that the ICME will cause considerable disturbances in the near-Earth space environment. For the superposed epoch analysis, the information about the number of sudden storm commencement follows the Richardson and Cane (2010) ICME catalog. Table S1 and S2 provide relevant information on those storms.

2.3 Plasmapause Dataset

Zhang et al. (2017) established a database recording the L shell of plasmapause, encompassing 49119 plasmapause crossing events of 18 satellites from 1977 to 2015. Based on this dataset, we analyzed the changes in the L shell of plasmapause during storms to search for possible plasmaspheric effects on the formation of strip-like bulge.

2.4 Bulge Observation and Extraction

Figure 1c presents a typical case, which shows the variation in plasma density with the QDLAT sampled by DMSP F13 at approximately 06:00 local time (LT) on 2 October 2002 during a storm. The bulge signature is snapshotted as two conjugated sharp density enhancements around the quasi-dipole latitude (QDLAT) of approximately ±30°, with longitudes of 136°E and 151.3°E. High-inclination low earth orbit (LEO) satellites are the major data source for identifying bulge signatures, and we previously reported that the bulge could occur persistently on several consecutive orbits, which results in the bulge behaving as a zonally strip-like structure (Wan et al., 2021; Wan et al., 2022). Based on these observation features, bulges during all the selected storms were manually collected from 11 adopted LEO satellites, yielding 7246 individual cases. In the rest of the paper, for those individual snapshotted cases, we refer it to as the bulge; but for the full zonally strip-like structure, we refer to is as the strip-like bulge.

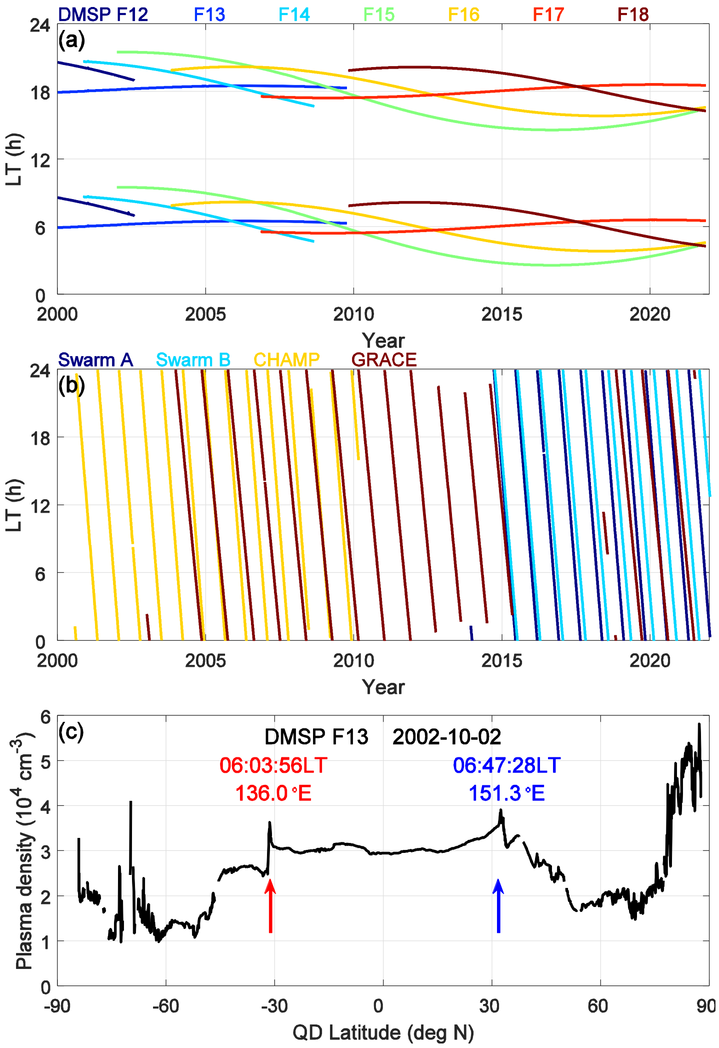

Figure 1. Local time variation of satellites orbit passes and a typical case of bulge observation. (a, b) Variation in orbits' local time over the equator for different satellites during 2000~2021, with different colors indicating different satellites. (c) Ion density versus QDLAT observed by DMSP F13 on 2 October 2002, bulges are marked with arrows.

3 Storm Features and Solar Activity Variation

After manual detection, bulges were observed in nearly half of the storms (61 storms) and missed in the remaining 75 storms, which raises the question of why the presence of bulges was not guaranteed in every storm.

Figure 2a shows the minimum SYM-H (minSYM-H) index of all the picked storms; those with bulges are highlighted in red. With or without the presence of bulges, the storms occurred throughout 2000~2021, with minSYM-H varying widely from -50 nT to minus hundreds of nT, suggesting that storm intensity is unlikely to determine bulge occurrence. However, during some periods, e.g., 2000~2005 and 2012~2016, the strongest storms are always registered with the presence of bulges. Moreover, during 2007~2010 and 2017~2021, storms were rare, but the presence of the bulge was almost 100%. To further quantitatively examine the probability, the occurrence rate of the bulge in each year is shown in Figure 2b, with the F10.7 solar flux set as a reference. The occurrence probability is clearly higher/lower during solar minimum/maximum, indicating an inverse correlation with the solar flux level. Therefore, bulges seem to favor storms during low solar activity periods but are still open to strong storms during high solar activity periods.

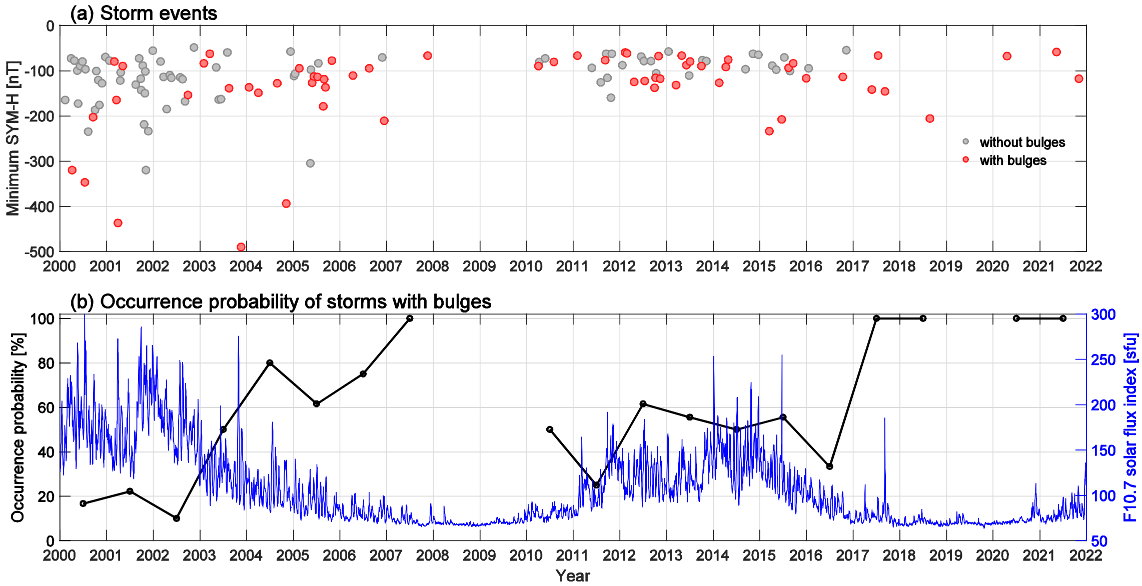

Figure 2. Occurrence of bulges varies with the storm intensity and solar activity. (a) The minimum SYM-H index of 136 storms during 2000~2022, with gray circles indicating storms without the bulge and red circles indicating storms with the bulge. (b) The black line is the yearly occurrence percentage for storms with bulges, and the blue line is the F10.7 solar flux index.

In Figure 3, we inspected several geomagnetic storm-related geospace indices to quantitatively evaluate the possible influence of storm intensity. The time axis was aligned when the SYM-H index reached its minimum (the UT of minSYM-H). The three columns represent three indices of the interplanetary magnetic field (IMF) component in the north-south direction (B_z), Aurora Electrojet (AE), and SYM-H. The top and middle panels show the results of the indices (gray curves) during storms with and without bulge occurrence, with averaging denoted by red and blue curves, respectively. The bottom panels show the differences between the two averaged profiles.

All three indices exhibit the same fluctuation ranges between the two categories (with and without bulges). Strong magnetic storms can be found in both categories, with B_z reaching less than -20 nT and AE reaching 2000 nT. In addition, SYM-H under conditions without bulges could reach -200 nT, although this value occurred less frequently than that under conditions with bulges. Therefore, no apparent threshold of storm intensity exists to account for the occurrence of bulge signatures.

Before the -24 h epoch, the difference in the indices between the two situations is generally at the same level as the residual values are approximately 0 nT (Figures 3c, 3f, 3i). This feature suggested that the pre-storm period indices maintain the same quiet time level for both storm categories. The situation changes as the epoch reaches the time of the minimum SYM-H. Geomagnetic storms accompanied by density bulges exhibit stronger B_z strengths than those without bulges by 8 nT. Similarly, in such cases, the maximum AE index is typically higher by approximately 250 nT, and the minSYM-H index is lower by approximately 30 nT. Therefore, from a statistical perspective, the occurrence of the bulge seems to favor stronger storms, although no clear boundary exists.

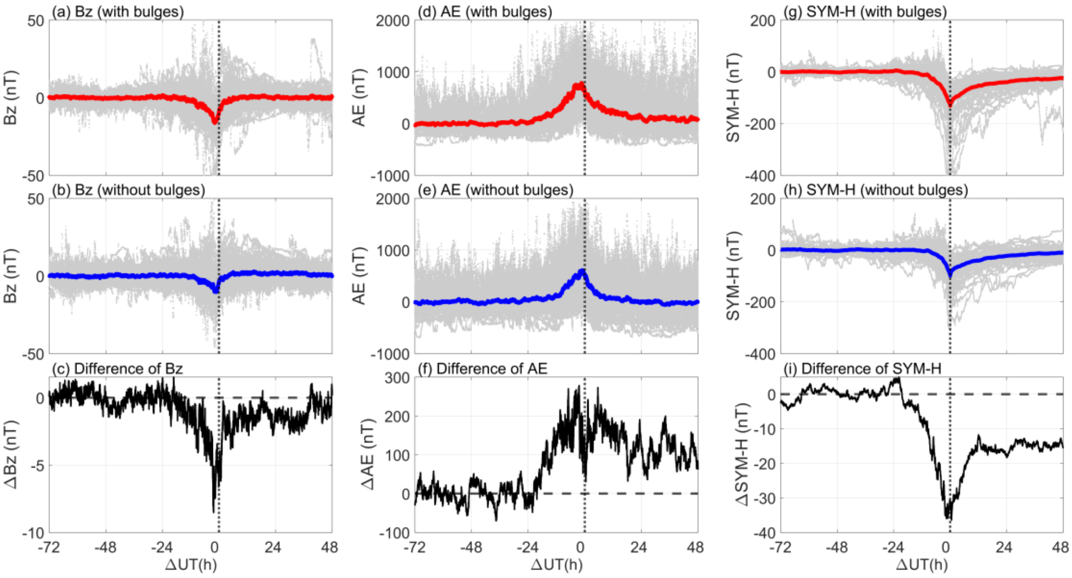

Figure 3. Differences in three geospace indices between the storms with and without bulges. The first row (a, d, g) and the second row (b, e, h) show the average B_z, AE index and SYM-H index versus time for storms with bulges (red) and storms without bulges (blue) from 2000 to 2021, respectively, and the light gray dots represent the variations in indices during individual geomagnetic storms. For each storm, data from five days are collected, and the background value is subtracted from the data (the average of the data from the first two days is taken as the background value). The third row (c, f, i) shows the difference obtained by subtracting the value of storms without bulges from the value of storms with bulges, and the horizontal dashed line marks the zero value. The vertical dotted line marks the time when the SYM-H index reached the minimum during storm time.

The angle between terrestrial and solar magnetic fields affects the rate of reconnection

(Russell & McPherron, 1973), which further influences the subsequent geomagnetic disturbances. Consequently, a semiannual variation exists, characterized by stronger geomagnetic storms near two equinoxes than the other seasons. Additionally, due to the angle offset between the magnetic and geographic poles, the impacts of geomagnetic storms on the thermosphere and ionosphere are known to exhibit universal time effect (Huang, 2013; Perlongo & Ridley, 2016; Wang et al., 2017) by controlling the energy deposit in the polar region (Lockwood, 2023) that further influences the global thermospheric circulation (Perlongo & Ridley, 2016; Wang et al., 2017) and affects the disturbance dynamo electric field (Huang, 2013). Based on the previous studies, we wonder whether the presence of bulges was associated with the seasonal and UT effects.

Figures 4a and 4b show the day of the year (doy) and UT information of those storms, with red and blue dots indicating storms with and without bulge occurrence, respectively. The UT variation in the storm is characterized by two epochs: the UT of SSC (sudden storm commencement) (Figure 4a) and the UT when the AE index first reaches 500 nT after SSC (Figure 4b). The latter epoch is selected because the AE can be used as a proxy for the substorm and quantify the ionospheric heating power (Østgaard et al., 2002). The critical 500 nT is set as an indication of the considerable intensity of the substorm and hemispheric power deposition. From the scatter plots (Figure 4a and 4b), both two types of geomagnetic storms occur in all seasons and exhibit no clear difference concerning their UT information. The percentages of the storm with bulges are shown in Figures 4c, 4d, and 4e. Still, no clear UT dependence could be identified (Figures 4c, 4d), but it exhibits an insignificant concentration occurring near the spring equinox season (Figure 4e). Overall, it seems the presence of bulges is not controlled by the seasonal and UT variations of geomagnetic storms.

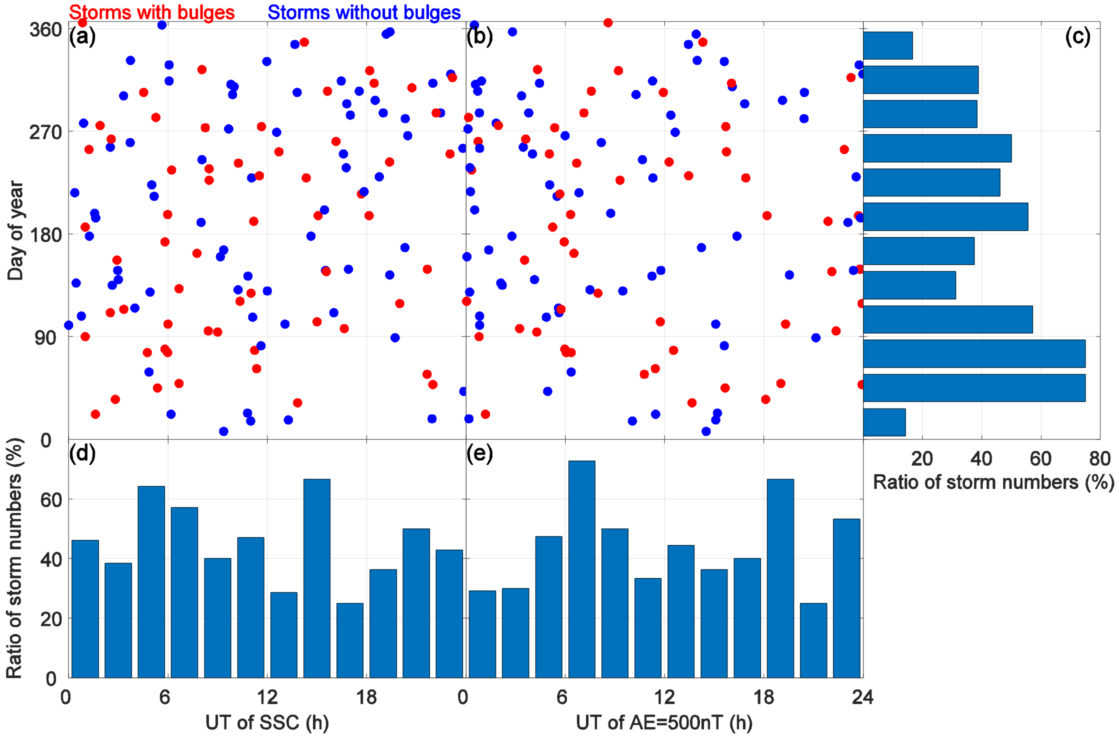

Figure 4. Storm information as a function of day of year and (a) the UT of SSC, or (b) the UT when AE first reaches 500 nT, the red dots represent the storms with bulges and the blue dots represent the storms without bulges. The percentage of the storms registered with bulge as a function of (c) day of year, (d) the UT of SSC, and (e) the UT when AE first reaches 500 nT, the ratio is obtained by dividing the number of storms with bulges by the total number of storms.

4 Spatial and Temporal Characteristics

4.1 Longitudinal Preference

Figure 5 displays the general longitudinal distribution of the bulges, due to the fact that the longitudinal coverages of the bulges vary from storm to storm (will be shown later) and we wonder whether it is associated with the storm intensity, the storm indices are also examined. Figure 5a shows the global occurrence rate of bulge. The values in the figure represent the probability of observing a bulge at a given location during the storms with bulges, calculated as the ratio of bulge observations to the number of satellites passing. The shaded area marks the region with a westward magnetic declination calculated with the CHAOS-7 model (Finlay et al., 2020). The bulges are predominantly distributed in the low-to-mid latitude regions in both the Northern Hemisphere (NH) and Southern Hemisphere (SH), exhibiting a symmetrical pattern. In addition, the bulge could occur at all longitudes but with several notable high-probability regions, including the east Asian-Pacific region and Atlantic-Europe region. The overall occurrence rate is higher in the eastward magnetic declination region than in the westward magnetic declination region. The highest probability of bulge occurrence can reach more than 4% in the vicinity of these regions. Figure 5b examines the number of storms when the bulges are found in the longitudinal bins. The bulges are concentrated in the range of 90°~240° E, with the number of storms reaching 55, while the number at other longitudes is approximately 40. Therefore, although the occurrence of the bulge has no limitation, some longitudinal preferences do exist. In other words, bulges seem to form more easily at longitudes.

The last section indicates that stronger storm intensity is favorable, we further examine this point from a longitudinal perspective in Figure 5c, which shows the minSYM-H and the first 24 h (after the storm onset) averaged AE index of the storms collected in Figure 5b. It can be clearly noted that the 24-h averaged AE index is lowest near 90°~240° E, corresponding to the most frequent occurrence of bulges, while the minSYM-H does not exhibit this feature. This means that for the longitude of 90°~240° E, bulges form more easily and do not require as strong geomagnetic disturbances as for other longitudes. In addition, the longitudinal occurrence feature seems to be more sensitive to the high-latitude AE index than to the equatorial SYM-H index. As mentioned previously in Section 3, AE is a good proxy for substorm-induced ionospheric heating power, which further drives global thermospheric disturbances. Therefore, this longitudinal preference highlights the intensity of the disturbance neutral wind as a controlling factor, which is consistent with the previously proposed pile-up scenario caused by the enhanced equatorward neutral wind (Wan et al., 2022; Wan et al., 2021) that pushes the plasma upward along the field lines. In addition, note that the magnetic declinations at the prevailing longitude of 150°~240° E are generally eastward in both hemispheres. In the NH, the neutral wind disturbance is mainly westward (Xiong et al., 2015), which contributes to upward field-aligned transportation. However, in the SH, westward disturbance wind would create the downward field-aligned transportation with eastward magnetic declination, which contradicts the upward pile-up scenario. Thus, additional electromagnetic forces might exist. This point will be examined later in Section 6.

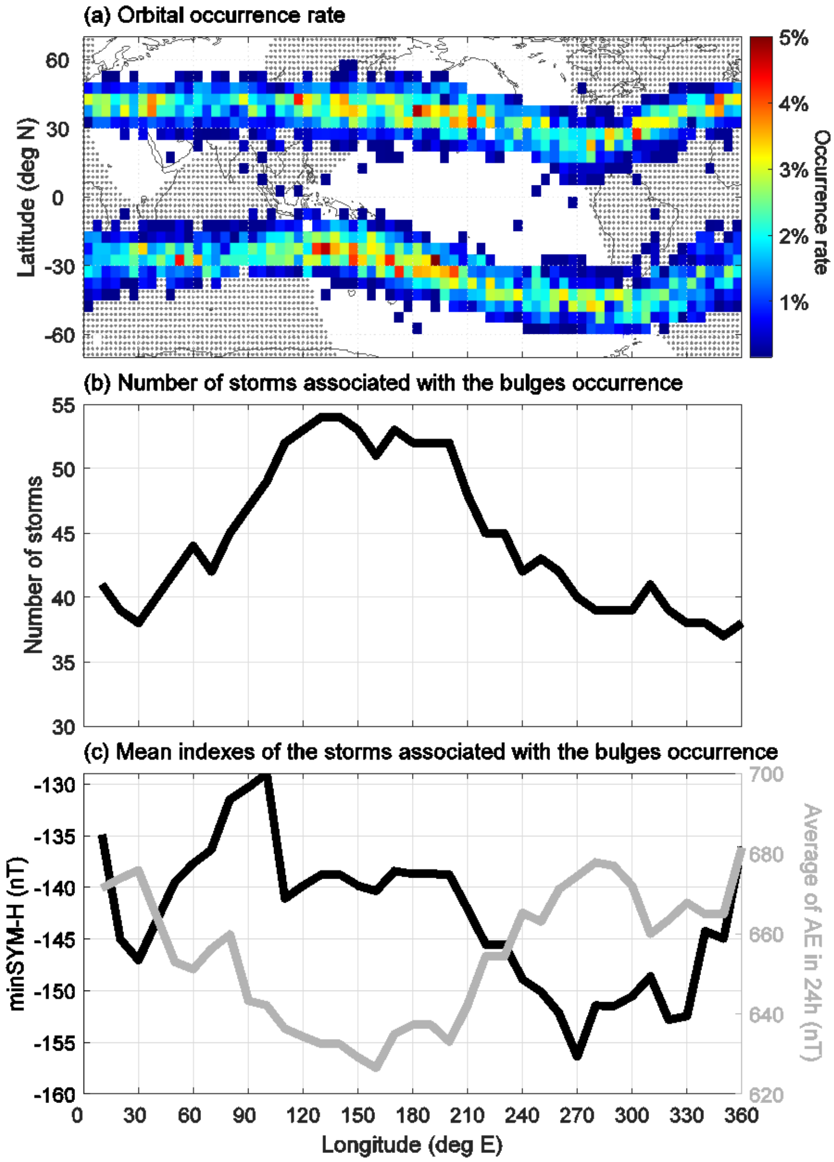

Figure 5. Overall longitudinal distribution of the snapshotted bulges and the storm features. (a) Occurrence rate map of the strip-like bulge, the shaded area represents the region with westward magnetic declination calculated with the CHAOS-7 model (Finlay et al., 2020). (b) Number of storms with strip-like bulges registered in each longitudinal bin. (c) The averaged minSYM-H and AE during 24 hours after the storm onset of the storms in each longitudinal bin for panel (b).

Furthermore, the individual bulge case is indeed a local 1-D snapshot of the entire longitudinally strip-like structure, so the eastern and western boundaries are needed to precisely constrain the longitudinal coverage of the strip-like bulges. Figure 6a shows two examples of bulge distributions during magnetic storms, which began on 19 November 2007 and 30 September 2012. The green triangles represent the observed bulges, while the black lines are the assumed continuous coverage. We focus on the regions where the bulge distribution is much denser than other longitude ranges with a resolution of 10°. The east and west boundaries of the bulges within these intervals can indicate a strip-like structure. The extraction process does not separate the Northern and Southern Hemispheres. The spans of the bulge are 130°~220° and 310°~130° E for the two cases.

Based on the above procedures, the central positions of the strip-like bulge for each storm event could be extracted and used for sortation. The sorting results are shown in Figure 6b. The red triangles represent the first appearance of the bulge, while the blue triangles represent the last appearance of the bulge. The longitudinal span of the bulges ranges from approximately 60° to a maximum of 270°, covering almost every longitudinal sector. Furthermore, the bulges often disappear at the west of their initial appearance. However, as Earth rotates from west to east, this feature might be an artifact that the satellite would naturally sample the bulge from east to west.

The aforementioned UT effects could also cause longitudinal dependence of the storm's impact on the thermosphere and ionosphere (Lockwood et al., 2021; Lockwood et al., 2020). For example, Immel and Mannucci (2013) showed that the American sector during the afternoon period exhibits, on average, greater storm time enhancement in ionospheric plasma content. We wonder whether the distinctive longitudinal extension of the bulges from storms to storms could also be influenced by this UT effect. Figure 6c and Figure 6d show the UT of SSC (sudden storm commencement) and the UT when AE reaches 500 nT, respectively, for each storm. The storm event serial number is the same as that on the Y-axis of Figure 6b. The colors of the data points correspond to the different months when the storms occurred, as denoted by the right-hand color bar. The scattered distribution of the points indicates the absence of a clear pattern, which suggests that the longitudinal distribution characteristics of the strip-like bulges are not influenced by the specific UT epoch associated with the storm or substorm phases or the seasons of the storms.

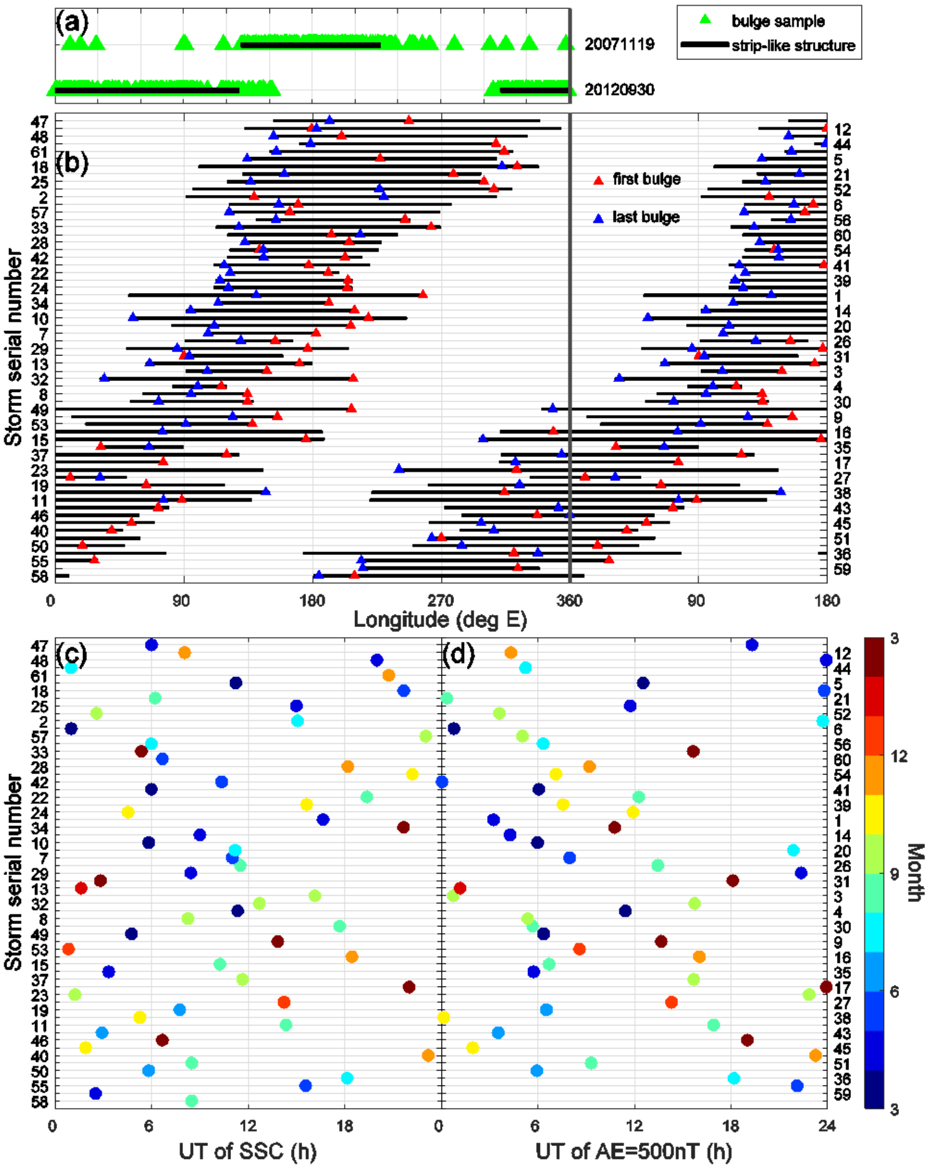

Figure 6. The zonal extension of the strip-like bulges in dfferent storm cases. (a) Strip-like structures (black lines) extracted from regional snapshots (red triangles) for two storm cases. (b) The sorting results of the strip-like bulges by their center positions. The first and last occurrences of bulges are indicated by red and blue triangles, respevtively. For easier visualization of the longitudinal extent, the range was extended beyond 360˚E to 180˚E, and the extended region was separated with vertical black lines. The characteristics of different geomagnetic storms corresponding to the (c) UT of SSC and (d) UT when the AE reaches 500 nT for the first time after SSC; months are represented by distinct colors.

4.2 Temporal Characteristics

In the temporal domain, bulges emerge during the main phase of storms, survive throughout the recovery phase, and persist for more than 48 hours (Wan et al., 2021; Wan et al., 2022). However, it is unclear whether the aforementioned longitudinal preferences change at different time epochs.

In Figure 7, we further conducted a superposed epoch analysis (SEA) to clarify the temporal and longitudinal evolution of the bulges. Due to the confirmed conjugacy feature of the bulge, Figure 7 no longer separates the northern and southern hemispheres. The white and black triangles represent the first and last occurrences of bulges, respectively, during each storm. The 0 h epoch is set as the time when SYM-H decreases to its minimum value after the SSC.

The bulges tend to emerge within 24 hours before the onset of the recovery phase of the storm. As the epoch passes 0 h, a significant increase in the occurrence of bulges can be observed for the next 24 hours across all the longitudes. Nevertheless, the boom of the bulge exhibits a concentration at longitudes of 90°~240° E, where a relatively longer duration can also be observed. The final presence of the bulge was mainly found 50 hours after the onset of the recovery phase. However, we note that the longitudes of bulges' first appearance and disappearance do not exhibit any distinctive features.

In addition, we tested other time epochs, such as the SSC, the first time when the AE reached 500 nT after SSC, and the first main peak of the AE after SSC; the results are shown in Supplemental Figure S1. The same burst of bulge occurrence across all the longitudes can also be observed but at approximately 20 hours after the 0 h epoch. Therefore, the minimum SYM-H seems to be the best reference for the temporal characteristics of bulges.

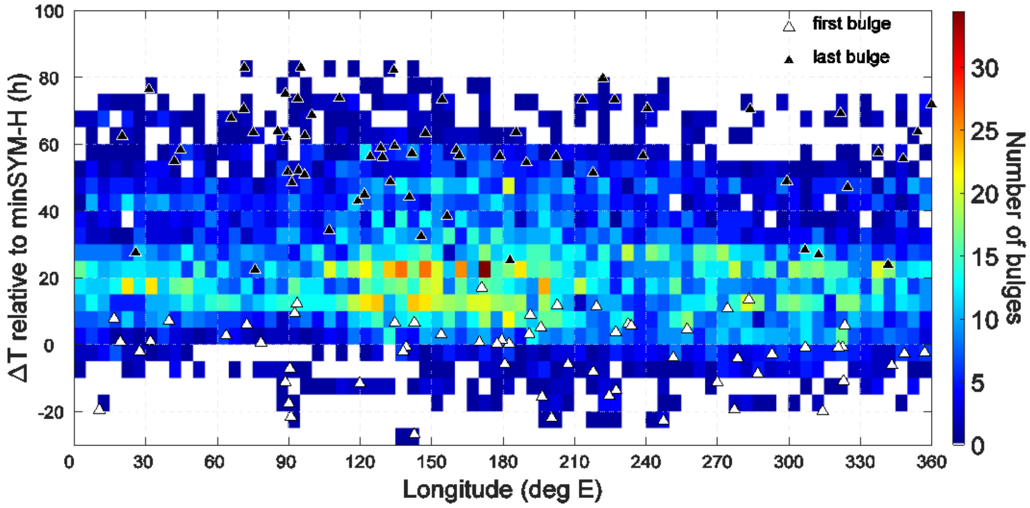

Figure 7. Superposed epoch analysis (SEA) of the occurrence number of bulges during magnetic storms at different longitudes. The 0 h epoch represents the moment when the SYM-H index reaches its minimum value. The white triangles represent the first occurrence of the bulge within a storm event, while the black triangles represent the last occurrence.

4.3 Local Time Preference

Figure 8 shows the occurrence rate of the bulges as a function of local time. The occurrence rate was calculated by the ratio of the number of orbits where bulges were observed to the total number of orbits. For storms with bulges, the total orbit number is calculated within the time range of the bulge occurrence, and for storms without bulges, the total number is calculated for five days following the start of the storm. Figure 8a displays the number of satellite orbits at different local times during storms. As expected, the satellites were mainly operating at dawn and dusk sectors for both storm categories, therefore, the local times dependence of bulges would not be affected due to the storm events differences. In Figure 8b, the occurrence rates are generally at a low level below 20%, which is due to the limited longitudinal coverage, thus the absence in some area, as noted in subsection 4.1. Nevertheless, the occurrence rate is highest near 20:00 and 04:00 LTs, which are both on the nightside near the dawn-dusk terminator, resulting in a day-night asymmetry.

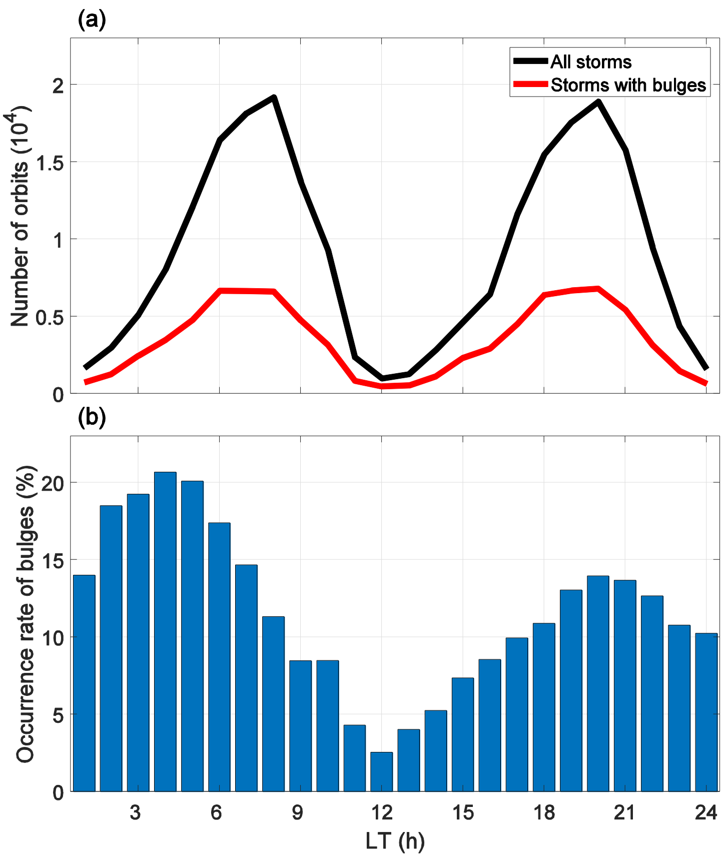

Figure 8. Local time variations of the satellites orbits and the occurrence of bulge cases. (a) Number of satellite orbits at different local times during all storms (black line) and storms with bulges (red line). (b) The value is obtained by dividing the number of orbits with bulges by the total number of satellite orbits in each LT bin during the storms with bulges.

In a short summary, this section conveys several occurrence features of the bulges: 1) bulges can appear in any longitude range but they are more likely to appear in the Asian-Pacific region; 2) bulges start to appear in the main phase of geomagnetic storms and boom in the recovery phase, which can last for about 60 hours; 3) bulges can appear at any local time but more favors the nightside of the dawn-dusk terminator.

5 Possible Precursor of Bulges

Previous studies captured a gentler but wider midlatitude density enhancement whose appearance does not require geomagnetic storms. The terminologies of this phenomenon include midlatitude enhancement (Rajesh et al., 2016), band structure (Zhong et al., 2019), latitudinal peaks(Xiong et al., 2019), and midlatitude extra peaks (Cai et al., 2022). Hereafter, we adopted the term "extra peaks" for this phenomenon. Wan et al. (2022) recognized this structure as the parent of a strip-like bulge, as a continuous shrinkage of the giant patch-like TEC enhancement was witnessed.

Figure 9 shows the method to extract the extra peaks and explores the possibility of them as precursors to bulges. A typical case is shown in Figure 9a. The gray line represents the plasma density observed by the DMSP F17 satellite near 22 UT on 6 April 2010, approximately 108° E, and two narrow bulges are marked with black vertical dotted lines. The red line represents the results for the nearby orbit from the same satellite on the previous day. Two bulge structures are symmetrically located near the 30° QDLAT in both the NH and SH, and two relatively smooth peaks were captured nearby on the previous day. This feature suggests that bulges might be converted from smoother peaks, supporting the previously proposed shrinking scenario (Wan et al., 2021). We further evaluated this point from a statistical perspective.

The first step is to extract the extra peaks before the storm. The "rolling barrel" method (Pradipta et al., 2015) was first applied to detrend the data. Analogous to a rolling barrel on an uneven surface, the method allows us to skip regions with sharp variations in the data and extract the envelopes. Figure 9a shows the extracted lower envelope of the data in the range of 15° to 50° latitude in both the Northern and Southern Hemispheres (the dashed lines). In practical operations, it is necessary to smooth and normalize the data before extracting it. We define the presence of extra peaks as the region enclosed between the lower envelope and the original data reaching a specific threshold value. However, this identification method may still lead to some misclassifications, so a manual inspection of all the extracted peaks was conducted to exclude unidentified cases. In this situation, authenticity is guaranteed, but there may still be some peak cases undetected. For storms with bulges, the midlatitude extra peaks were extracted one day before the first occurrence of the bulge, and for storms without bulges, we extracted the extra peak one day before the onset of the storm.

Two methods exist for evaluating the possible relationship between these two phenomena. One is forward tracing: Select all the extra peaks before the storm, and trace the bulges during the following geomagnetic storm. The other way is backward tracing: selecting all the bulges during storms and tracing the extra peaks before the storms. In practice, if the bulges and the extra peak occur within 10° of longitude, it is recognized as tracked. Figure 9b shows the traceability rate of the bidirectional tracing during storms with bulges. The tracing rate reached 64% and 95% for the forward and backward tracing scenarios, respectively. This means that the bulges are almost definitely originated from the extra peaks, while the extra peaks could frequently but will not definitely lead to the birth of the bulges.

The longitudinal distribution of the storms with peaks with the bulge appearance is shown in Figure 9c. Moreover, there was no significant difference between the NH and SH. The corresponding events are primarily concentrated at 90°~240° E, with the number reaching 100, while other regions are at a level of approximately 80. This characteristic is similar to the longitudinal distribution of the bulges (Figure 5b). Figure 9d shows the storms without bulges. In the NH, the distribution exhibits significant fluctuations, with higher frequencies occurring at 120°~300° E, reaching more than 50. In the SH, the frequency is notably lower at 300°~30° E than at other longitudes. This longitudinal dependence is less similar to the distribution of the strip-like bulge. Therefore, the longitudinal dependence of the strip-like bulges is also influenced by the midlatitude extra peaks.

Figure 9e displays the occurrence frequency of the extra peaks before each storm, the red bars represent storms with bulges, and the blue bars represent storms without bulges. The peak number for storms with bulges is significantly greater than that for storms without bulges.

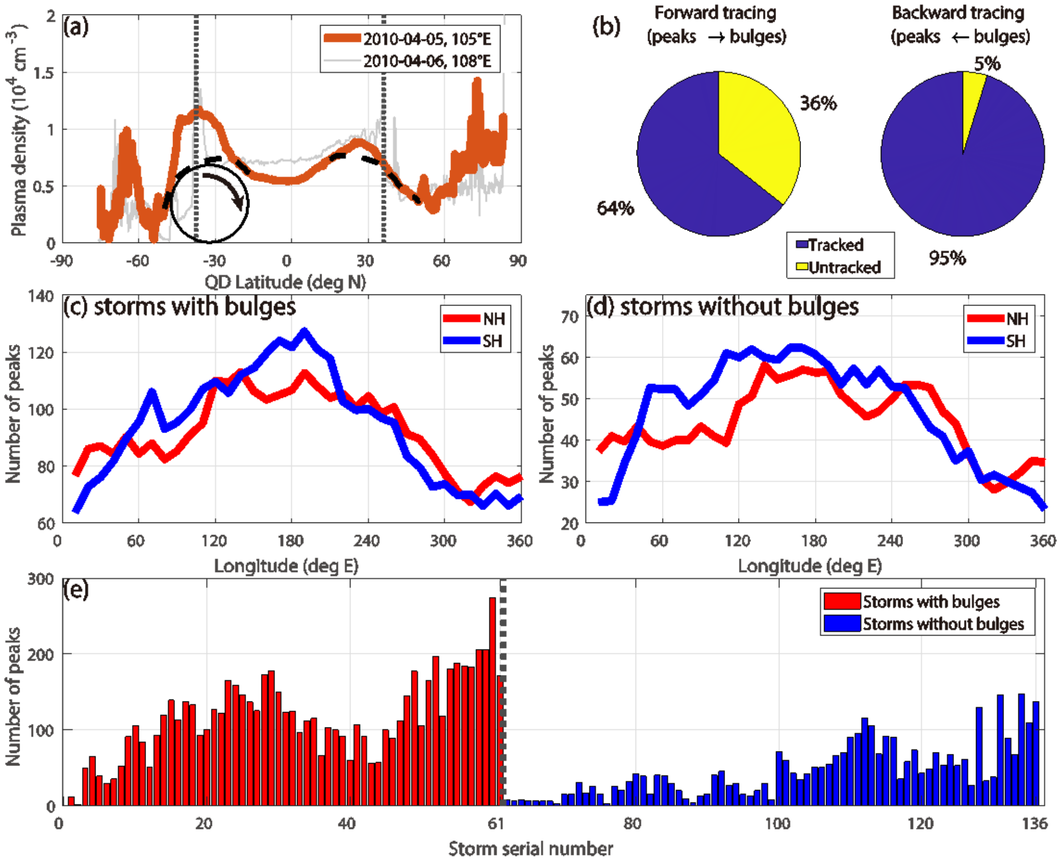

Figure 9. Relation between bulges with midlatitude extra peaks. (a) Plasma density versus QDLAT observed by DMSP F17 at 22 UT on 6 April 2010 (gray line, showing bulges case) and at 22 UT on 5 April 2010 (red line, showing extra peaks case). The latitude of the bulge is indicated by dotted vertical lines, and the lower envelope of the data in the range of 15°~50° is shown as black dashed lines. (b) The tracing rate between the bulges and the peaks. Number of peaks before storm in each longitudinal bin during (c) storms with bulges and (d) storms without bulges. (e) Case numbers of the extra peaks before the storms for those with bulges (red) and without bulges (blue).

6 Possible Formation Mechanism

The above results have two indications: 1) the extra peaks and bulges are essentially the same; 2) the two structures are not the same, but the presence of the extra peaks indicates a shared favorable background condition for initiating the strip-like bulge. The latter indication is due to the constitutional difference between the two structures. The midlatitude extra peaks could be observed down to the CHAMP altitude below 400 km (Zhang et al., 2024), indicating that the ionospheric O^+ plays a dominant role. In addition, we examined several DMSP extra peak cases and found O^+ dominance (not shown). However, bulges during the 7-8 September 2017 storm were found purely by H^+/He^+ (Wan et al., 2021). Therefore, the second indication seems more reliable. Nevertheless, for either indication, the formation scenario associated with the converting of extra peaks and the plasmaspheric compression is still effective. However, the formation scenario is inferred from the evidence provided by case studies (Wan et al., 2021; Wan et al., 2022) that might reflect a sporadic phenomenon; thus, statistical confirmation is needed.

6.1 The Ion Composition

In Figure 10, we explore the ion composition of bulges. The ion compositions of H^+/He^+ and O^+ densities measured by DMSP satellites were collected. When the satellites pass over the bulge, we extract data within the 3° QDLAT on both the northern and southern sides of the bulge and calculate $n(H^+)/n(O^+)$ before and during geomagnetic storms. Each profile obtained along a single orbit was further normalized. The average of all the normalized profiles is shown in Figure 10a. Before the storm, the $n(H^+)/n(O^+)$ at low latitudes is greater than that at high latitudes in both hemispheres. However, during a storm, $n(H^+)/n(O^+)$ is always greater at the bulge position than on both sides (north and south), and the ratio decreases more rapidly at higher latitudes than at lower latitudes around the bulge, indicating that $n(H^+)/n(O^+)$ significantly increases with the appearance of bulges.

Figure 10b displays the number of bulge cases as a function of $n(H^+)/n(O^+)$, where the red and blue bars represent the data obtained within the bulge and the surroundings, respectively. The surroundings are defined as the regions 5° QDLAT away from the center of the bulge. The $n(H^+)/n(O^+)$ value typically falls within the range of 0.1 to 10, with considerable cases for both the $n(H^+)/n(O^+) > 1$ and $n(H^+)/n(O^+) < 1$ conditions. In the NH, there are relatively more bulges with $n(H^+)/n(O^+)$ less than 1, whereas in the SH, there are relatively more bulges with $n(H^+)/n(O^+)$ greater than 1. Furthermore, $n(H^+)/n(O^+)$ in the surroundings is significantly lower than that in the location of the bulge. This indicates that the H^+ density in bulges is generally higher than that in their surroundings, but it does not necessarily need to exceed the O^+ density. In other words, bulges are more likely plasmaspheric structures that intrude downward into the ionosphere.

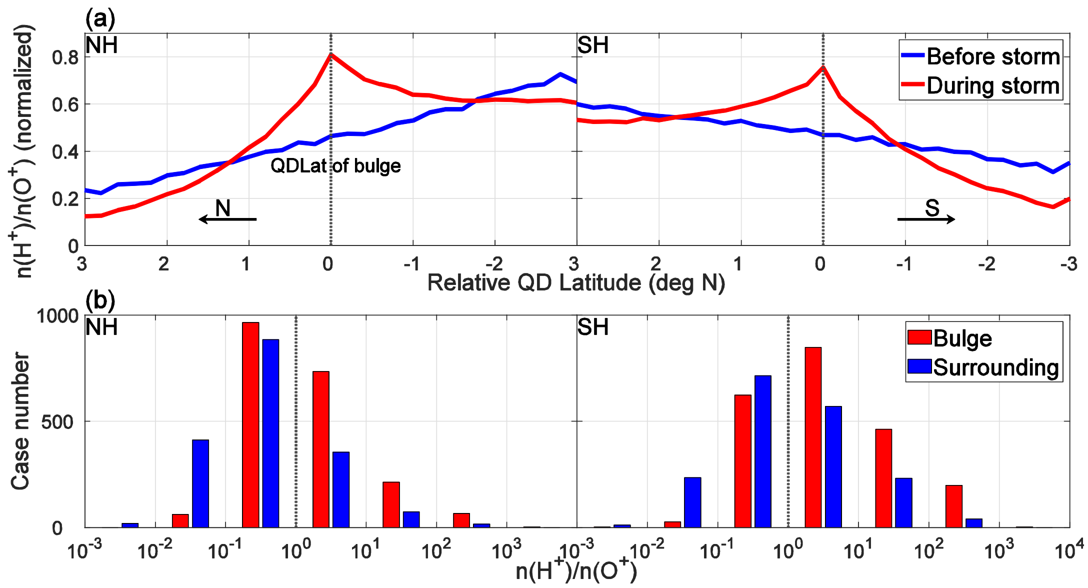

Figure 10. Ion composition features. (a) Normalized $n(H^+)/n(O^+)$ around the bulge position (red line) as a function of relative QD latitude with 0° being the center of the bulges, the blue lines are the quiet time references. (b) Histogram of the bulge case number as a function of $n(H^+)/n(O^+)$ near the peak of the bulge (red) and the surroundings (blue); the vertical dotted line marks the value of 1. The two columns represent the data from the Northern Hemisphere and the Southern Hemisphere, respectively.

6.2 The Plasmaspheric Compression

The above results prove that the formation of the bulge is related to the invasion of the overlying plasmaspheric light ions, which indicates a downward H^+stream at the lower middle latitude. Storms could lead to significant erosion/compression of the plasmasphere, and the presence of a convection electric field that penetrates from high latitudes to middle latitudes might further exacerbate compression (Obana et al., 2019). That indicates that the earthward movement of the plasmapause might provide additional evidence of H^+stream invasion into the ionosphere.

Figure 11a~f illustrates two storms with the highest AE index reaching more than 1000 nT and the lowest SYM-H index reaching -60 nT. For the storm with bulges, the L shell of plasmapause decreases from 5 to 3 within 24 hours after storm onset at approximately 3:00 and 20:00 MLT. In contrast, the compression of the plasmasphere associated with a storm without bulges is more moderate. After the storm eruption, the L shell at 1:00-3:00 MLT changes from 5 to 4. The L shell of the plasmapause decreases by 2 during the storm with bulges, whereas it decreases by 1 during the storm without bulges.

Figure 11g shows the SEA of the L shell during two sets of magnetic storms (with or without bulges). To ensure that the geomagnetic storm samples are both sufficient and have similar storm intensities, we selected storms with minimum SYM-H values ranging from -200 to -100 nT. To eliminate the influence of different MLTs, the median L shell value is taken for each specific moment in time. It indicates the difference between the two types of storms. Compared to storms without bulges, plasmapause of storms with bulges often exhibit more quiet time, and the degree to which the plasmapause descends is more severe by approximately 0.5 L shell. We also tested the selected storms with minimum SYM-H values ranging from -100 to -50 nT, and similar results (not shown) were obtained.

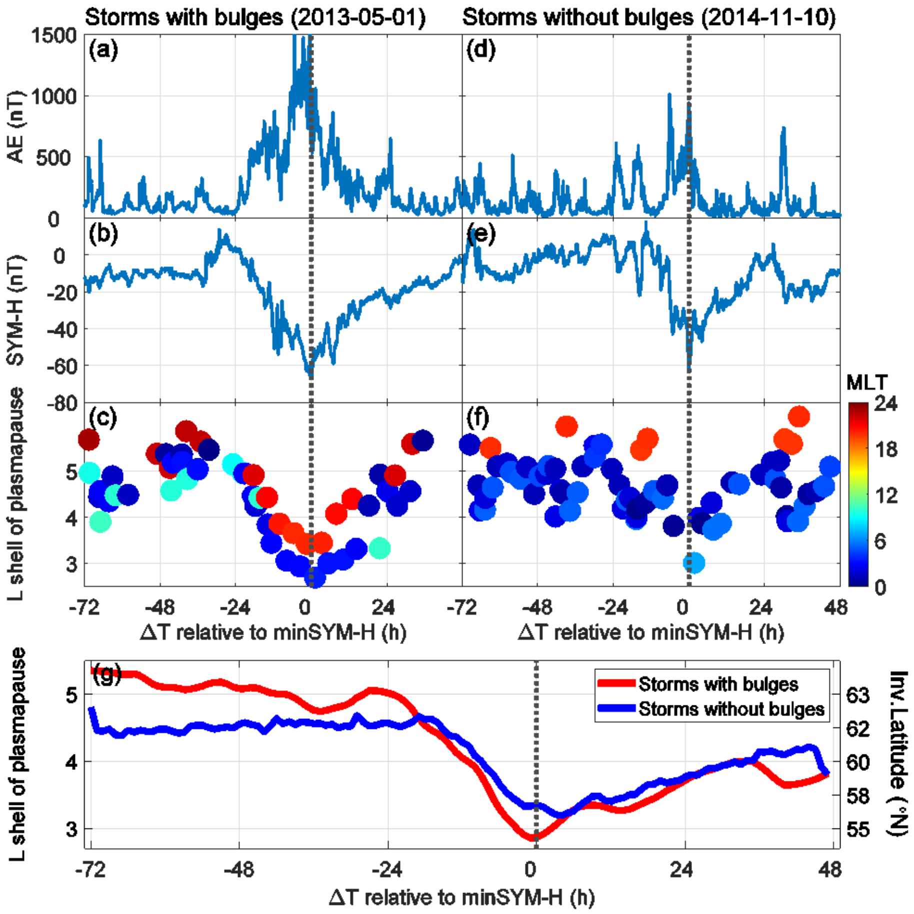

Figure 11. Temporal variations of the plasmapause L shell. Left and right column represent storm case occurred on May 1, 2013 and November 10, 2014 storm, respectively, when the bulges were presented and not presented. The AE index (a and d) and SYM-H index (b and e) are shown as references. The MLT information of the plasmapause L shell in (c) and (f) is denoted by different colors. (g) Median L shell (corresponding invariant latitudes are indicated on the right) of the plasmapause during storms with (red) and without (blue) density bulges. The dotted line indicates the UT of minSYM-H during the storms.

The variations of the plasmaspheric dynamics are known to exhibit magnetic local time

(MLT) effects, we wonder whether these effects influence the bulges. Figure 12 shows the L shell of the plasmapause versus the UT during storms with bulges for different MLT intervals. The data points in Figure 12 were obtained by extracting the median value from different MLT intervals (shown as different colors in Figure 12e) within different UT intervals during different storm events. The solid line in the figure represents the smoothed data obtained from the points. The L shell of the plasmapause at different MLT intervals was normalized for analysis. There is evident compression of the plasmapause within each MLT interval, but the decrease in the plasmapause L shell during 00:00~06:00 MLT (Figures 12a and b), 09:00~12:00 MLT (Figure 12d) and 18:00-24:00 MLT (Figures 12g and 12h) is greater than the rest three MLT sectors. We remember that the occurrence rate of bulges is also strongest on the nightside (Figure 8), suggesting that severe plasmaspheric compression might contribute to the strip-like bulge. The additional cross-L inward motion of the plasmasphere (Obana et al., 2019) might also contribute to this difference.

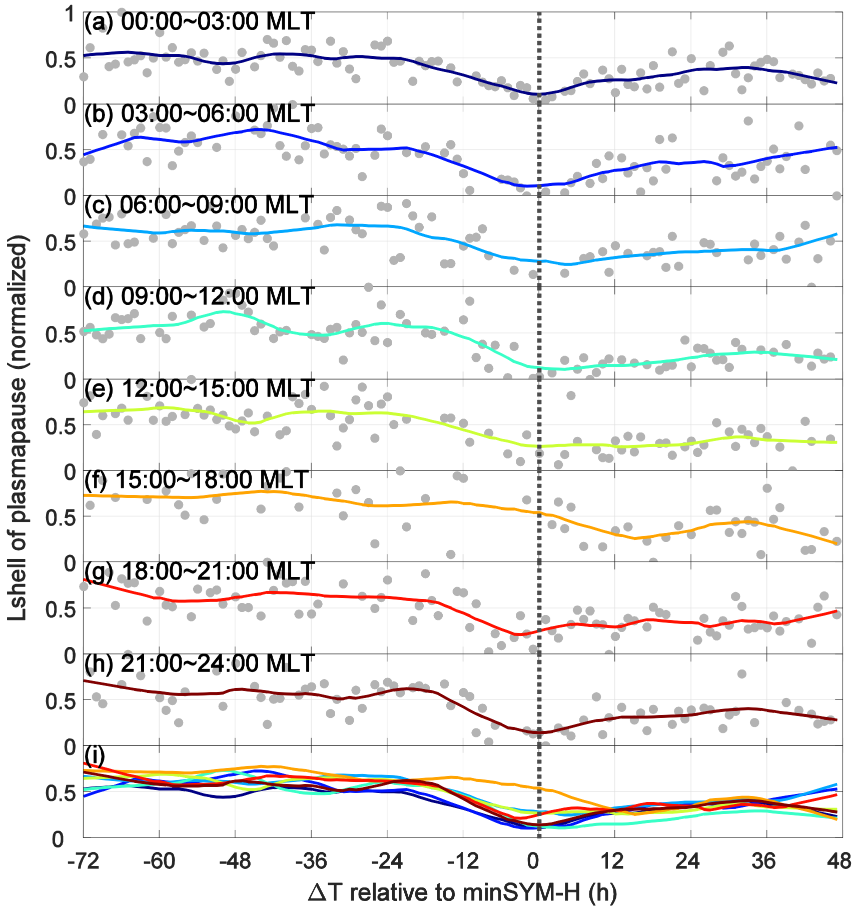

Figure 12. Normalized L shell of plasmapause versus the UT during storms with bulges, for (a-h) different MLT intervals. The dots in the graph represent the data points, while the solid line represents the smoothed data. (i) shows all solid lines for different MLTs with different colors. The dotted vertical line indicates the time of minSYM-H.

6.3 Ion Drift Features

The ion drift observations may provide direct evidence to illustrate the field-aligned downward and cross-L inward ion motion on the formation scenario of the strip-like bulge. The DMSP satellite can measure ion drift in three directions: vertical crosstrack drift, horizontal crosstrack drift, and ram drift. Due to the poor quality of the ram drift data, the remaining two components are considered to be converted to local magnetic coordinates with CHAOS-7 model (Finlay et al., 2020). The field-aligned component is referred to as Va, with the positive direction pointing north; the component within the magnetic meridional plane and perpendicular to the field line is referred to as Vp, with the positive direction pointing upward/outward.

Figure 13 displays the derived ion drift observed at the bulge location at different local times and longitudes (shaded area). Figures 13a and 13b show a case that Va and Vp exhibit no significant changes at the bulge location, but some apparent local variations can be observed (Figures 13c~13h). Note that due to the lack of data on the ram velocity, the absolute magnitude of the converted ion drift is meaningless, but the local variation should provide additional information. For instance, Figures 13c and 13d show that the Vp is generally negative and decreases inside the bulge for both hemispheres, which means that the cross-L inward ion drift is stronger inside the bulge than in the ambients, thus indicating a net inward velocity. Moreover, Va increases and decreases in the NH and SH, respectively, reflecting two downward net streams in both hemispheres. However, the two drifts in Figures 13e and 13f exhibit upward and outward net velocities in both hemispheres, which is opposite to the situation shown in Figures 13c and 13d. In Figures 13g and 13h, Va is enhanced in both hemispheres, suggesting a continuous northward net field-aligned flux, whereas Vp exhibits opposite variations in two hemispheres, that is, the net inward/outward in the NH/SH. Therefore, the ion drift pattern seems to vary for different bulge cases.

To statistically evaluate the ion drift configuration, we define a drift fluctuation index (DFI): the difference between the sum of the drift velocity gradient on the south side and the north side within the 2° QDLAT of the bulges' peak. The calculation is given by equation (1):

$$DFI = \frac{1}{2} \times \left(\sum_{south} \frac{d(V)}{d(QDLat)} - \sum_{north} \frac{d(V)}{d(QDLat)} \right) \#(1)$$

The DFIs of each bulge are also given in Figure 13. For the case where the ion drift exhibited no clear variation, the |DFIs| were less than 90 (Figure 13b), whereas the |DFIs| varied from 188 to 2474 for the remaining bulge cases. In addition, the polarity of DFI well reflects the enhanced or decreased features of the ion drifts. Therefore, the index could be used to illustrate the occurrence of simultaneous ion drift disturbances and quantify the net ion velocity.

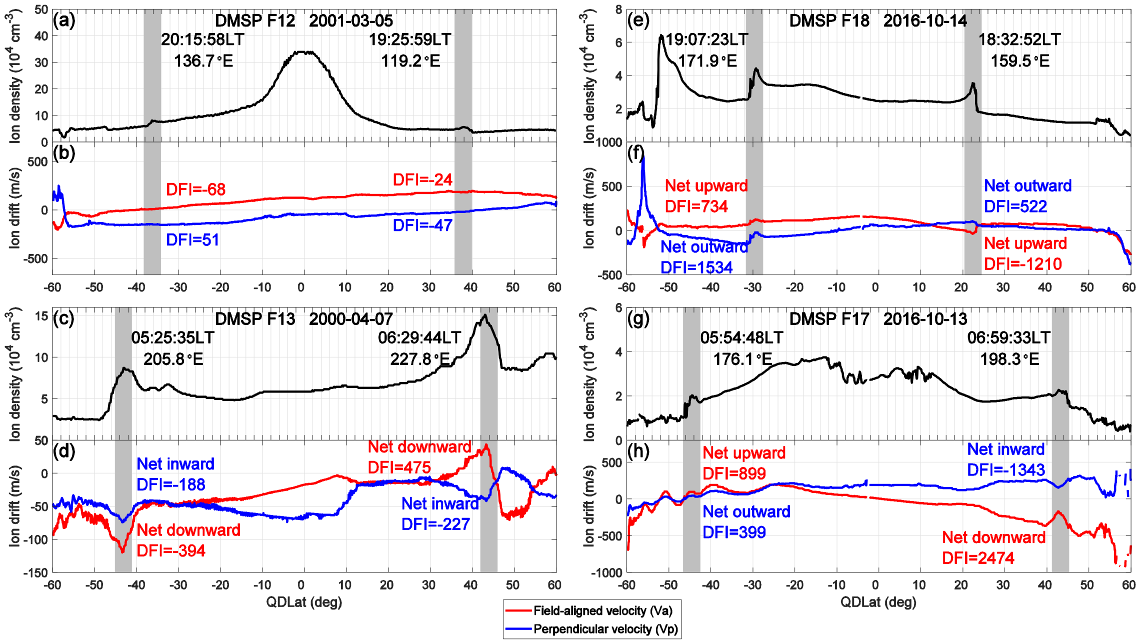

Figure 13. Four cases of ion density (a, c, e, and g) and ion drift (b, d, f, and h) measured by the DMSP satellite at different local times and longitudes. In the figures of ion drift, the red line represents the field-aligned velocity (Va), and the blue line represents the perpendicular velocity (Vp) in the meridional plane of the magnetic field lines. The shaded areas highlight the bulges, the corresponding ion drift fluctuation index (DFI), and the indicated net ion drift directions.

Figure 14 displays the DFI_{va} and DFI_{vp} in the NH and SH to investigate the ion drift disturbance. The values (DFI_{va}, DFI_{vp}) of the bulge cases in the NH are first mapped in a rectangular coordinate, as shown in Figures 14a and 14c, separated by dawn and dusk sectors due to the orbital characteristics of the DMSP. DFI_{va} and DFI_{vp} could appear in all four quadrants, indicating the presence of four types of net drifting configurations, as denoted by the four simplified sketches marked with Roman numerals. The bulge events in different quadrants are categorized by different colors. According to the categories (quadrants) of the bulge events (i.e., the (DFI_{va}, DFI_{vp})) in the NH, we then return to the same orbital profile to extract (DFI_{va}, DFI_{vp}) in the SH and map them in separate coordinates (Figures 14b and 14d) with same colors. The event numbers and percentages are also shown for each quadrant.

As we can see, under all circumstances, (DFI_{va}, DFI_{vp}) can always be found in all four quadrants, indicating the presence of complex net ion drifting patterns, that is, 16 different patterns concerning both the NH and SH. Setting a DFI threshold of 90 to define whether there exist clear local ion drift disturbances, it turns out that the ion drift disturbances are missed for approximately half of the bulge events. Nonetheless, DFI_{va} and DFI_{vp} are generally negatively/positively correlated in the NH/SH, regardless of the local time sector, representing two prevailing net drifting patterns for both hemispheres: 1) field-aligned upward and cross-L outward, 2) field-aligned downward and cross-L inward. In the dawn sector, the most dominant pattern is the field-aligned downward and cross-L inward (type IV in Figure 14a and type VII in Figure 14b), accounting for 39%. In the dusk sector, the two prevailing patterns exhibit similar proportions of approximately 16% (type I in Figure 14c and type VI in Figure 14d; type IV in Figure 14c; and type VII in Figure 14d).

The overall greater occurrence of downward/inward ion motion in the dawn sector supports the formation scenario associated with stronger storm time plasmaspheric compression (Figure 11), which further contributes to bulges (Figure 8). This feature is consistent with a historical Millstone Hill incoherent scatter radar (ISR) observation during the 7 July 2000 storm, that is, the field-aligned upward/downward appears in the inner/outer flux tube near the density enhancement (Foster & Coster, 2007). Furthermore, this scenario is also exactly the same as the shrinking or the narrowing process that converts the extra peaks to strip-like bulges. The specific dynamics are characterized by an equatorward turning of ion drift at the poleward side of the strip-like bulge (Wan et al., 2022), which further contributes to the field-aligned upward flux, thus, a net downward flux within the bulge. Note that the ISR observation was near the dusk sector, whereas our results show that the net ion drift in the dusk sector could also be outward/upward, and this feature clearly does not support the plasmaspheric compression scenarios. Thus, the downward/inward net ion motion in the dawn sector might be a favorable but not necessary condition to help form the strip-like bulge. However, this dawn-dusk difference in the prevailing net ion drift patterns remains unexplained.

A similar problem is that more than 60% of DMSP orbits exhibit other diverse (or no) net ion drift patterns concerning the bulge pair in conjugate hemispheres. In other words, the net ion drift pattern within the bulge flux tube is not exclusive but varies from orbit to orbit, making it inappropriate to yield cause-effect interpretation. We suspect that this difference is due to the timing of the bulges concerning their evolution. That is, different processes might dominate different stages of the strip-like bulge, as the storm time prompt penetration electric field and disturbance dynamo electric field dominate different storm phases (Fejer & Scherliess, 1995). Similarly, as shown in Figure 14, we examined the net ion drift configuration at different times when bulges first appeared, but the results showed no clear timing effect (Supplemental Figure S2).

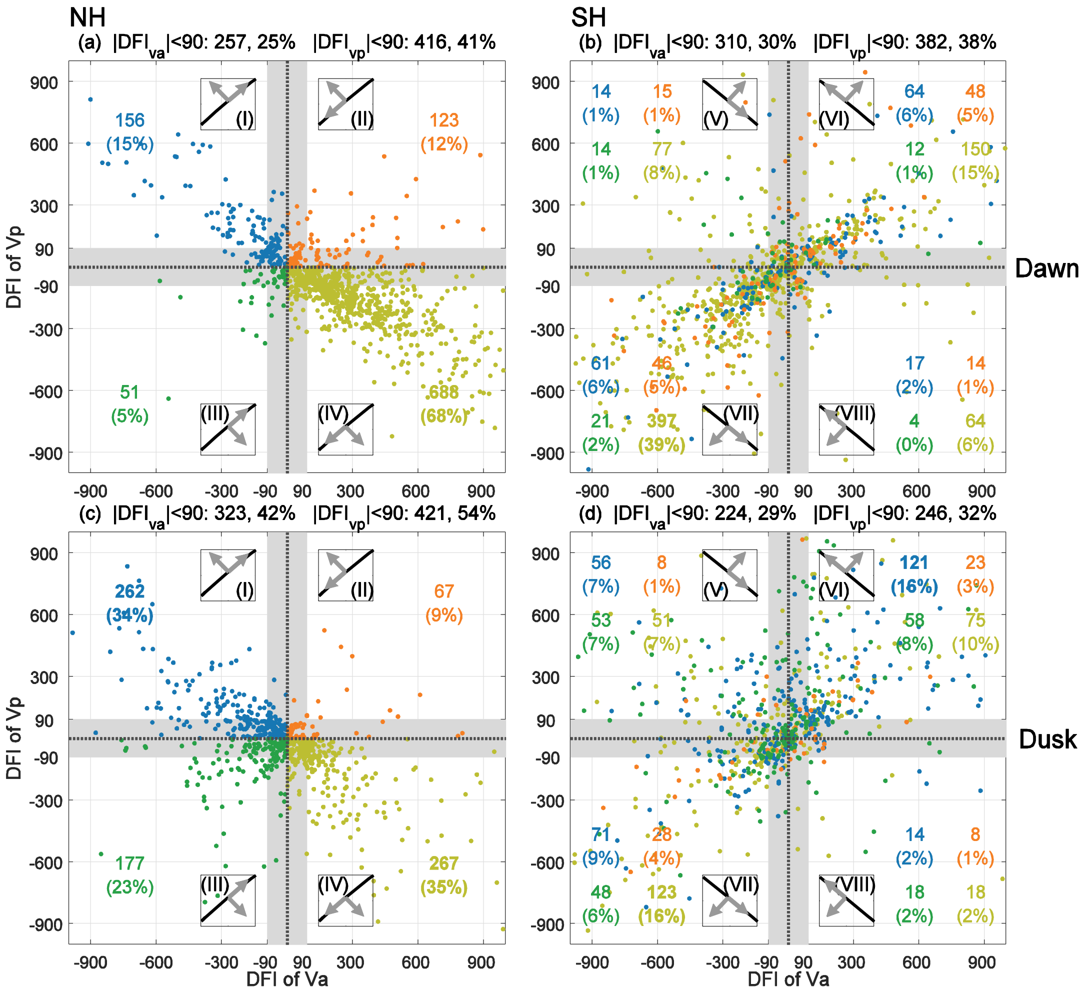

Figure 14. DFI of field-aligned ion velocity (Va) and perpendicular ion velocity (Vp) at the bulge location in different hemispheres and local time sectors. The first row (a-e) represents the dawn sector (3~9 LT), and the second row (f-j) represents the dusk sector (15~21 LT). The number of events with DFI less than the threshold of 90 is texted in the title. The first column (a, f) represents the DFI of the bulge in the NH, where cases in different quadrants are represented by different colors and the number/percentage of cases is indicated; simplified sketches of the net ion drift configurations are presented in the attached box, with the black line being the magnetic field line and the gray arrows denoting the two net drifting components. The second column shows the SH data; the same color between the NH and SH data indicates that the DFIs were derived from the same orbital profiles.

In summary, we infer that after the onset of a geomagnetic storm, the plasmasphere is compressed, causing H^+/He^+ in the plasmasphere to invade the ionosphere and form the bulge structure. This scenario is supported by the the ion drift pattern at the dawn sector in field-aligned downward/cross-L inward directions, but this feature is not obvious at the dusk sector.

Nonetheless, all these features suggested that the bulge appears probabilistic in nature and capable of emerging under diverse ion drift configurations, with downward/inward or upward/outward flux being more favorable than usual. This situation is similar to the above-presented occurrence rate dependence on the longitude, storm intensity, local time, or solar cycle. Why ion drift exhibits such a difference and whether this difference is associated with instrumental errors are currently unknown. In the future, we intend to conduct a more in-depth multi-instrumental analysis of different storm events to provide a solid clarification.

7 Conclusions

In this study, we adopted 136 ICMEs-driven geomagnetic storm events with 11 Polar-orbiting satellite observations during 2000~2021 to statistically investigate strip-like bulges, revealing a number of new occurrence features of the strip-like bulges, as listed below:

1. The occurrence of the bulge has no strict limitation on the longitude, storm intensity, local time, or solar cycle but does prefer the Asian-Pacific sector (eastward magnetic declination), stronger storms, nightside of the dawn-dusk terminator (near 20:00 and 04:00 LT), and solar minimum periods.

2. The longitudinal coverage of strip-like bulges varies from storm to storm, but strip-like bulges more easily form at their prevailing longitudes (i.e., Asian-Pacific sector), which have lower substorm intensity requirements and survive longer.

3. Bulges emerge predominantly near the end of the storm main phase and can be preserved for more than 60 hours.

4. The presence of the bulge cases could always be tracked backward by the midlatitude extra peaks that occur before storm onset, whereas the quiet time extra peaks have a large chance, but not always, to lead to the presence of the strip-like bulge.

5. Strip-like bulges could appear both below and above the transition height of the ionosphere and plasmasphere, but the dominant ion composition is always H^+/He^+,

suggesting that it is essentially the plasmaspheric structure that intrudes into the ionosphere.

6. The plasmaspheric compression shares some similarities depending on the storm intensity or local times with the strip-like bulges, indicating a possible contribution made from the plasmaspheric cross-L inward ion drift.

7. The local net ion drift regarding the ambient flux tube has diverse patterns from case to case, but at the dawn sector, it is mainly the field-aligned downward/cross-L inward.

A previously proposed formation scenario is characterized by an enhanced equatorward disturbance of neutral wind that pushes the plasma upward along the field lines at the poleside, to squeeze the midlatitude extra peak into the strip-like bulge, aided with additional cross-L inward plasmaspheric compressions (Wan et al., 2021; Wan et al., 2022). From many aspects, the above statistical features support this scenario. Furthermore, the local net ion drift configuration of field-aligned downward/cross-L inward could be regarded as direction evidence. However, why does the net ion drift exhibit another less popular configuration of field-aligned upward/cross-L outward? Another problem is that in addition to the above two configurations, many other minority configurations exist for the two ion drift components concerning the bulge pairs in both the Northern and Southern Hemispheres. Why does the net ion drift exhibit such diverse patterns? Are those unexpected drifting patterns true, and how would they contribute to the formation of the strip-like bulge? We hope that future in-depth multi-instrumental analysis will help to answer this question.

Acknowledgments

This work was supported by the National Natural Science Foundation of China (42374181, 42374186, 42104169, 42104147, 41804150, 41804153), Guangdong Basic and Applied Basic Research Foundation (2021A1515011216, 2022A1515011580, 2020A1515110242), the Strategic Priority Research Program of Chinese Academy of Sciences (XDB41000000), the Joint Open Fund of Mengcheng National Geophysical Observatory (No. MENGO-202217), Science and Technology Project of Shangrao City (2021F002), the Natural Science Foundation of Jiangsu Province (No. BK20180445), Key Laboratory of Tropical Atmosphere-Ocean System (Sun Yat-sen University), Ministry of Education, the Fundamental Research Funds for the Central Universities, the Opening Funding of Chinese Academy of Sciences dedicated for the Chinese Meridian Project, the Open Research Project of Large Research Infrastructures of CAS - "Study on the interaction between low/mid-latitude atmosphere and ionosphere based on the Chinese Meridian Project".

Data Availability Statement

Swarm data are provided by the European Space Agent (https://earth.esa.int/web/guest/swarm/data-access). DMSP data are provided by the National Centers for Environmental Information (https://satdat.ngdc.noaa.gov/dmsp/). The CHAMP electron density data (product identifier: CH-ME-2-PLPT) are available at the Information System and Data Center of Helmholtz-Center Potsdam—German Research Center for Geosciences (GFZ) (ftp://anonymous@isdcftp.gfz-potsdam.de/champ/ME/Level2/PLPT). GRACE KBR observation files are available at (ftp://isdcftp.gfz-potsdam.de/grace/IONOSPHERE/KBR_Electron_Density/0101).The solar wind and geomagnetic indices can be accessed in the GSFC/SPDF OMNIWeb database (https://omniweb.gsfc.nasa.gov/). The CHAOS-7 model is provided by the Technical University of Denmark (http://www.spacecenter.dk/files/magnetic-models/CHAOS-7/).

References

Cai, X., Qian, L., Wang, W., McInerney, J. M., Liu, H. L., & Eastes, R. W. (2022). Investigation of the Post-Sunset Extra Electron Density Peak Poleward of the Equatorial Ionization Anomaly Southern Crest. *Journal of Geophysical Research: Space Physics, 127*(10), e2022JA030755. https://doi.org/10.1029/2022ja030755

Chartier, A. T., Datta-Barua, S., McDonald, S. E., Bust, G. S., Tate, J., Goncharenko, L. P., Romeo, G., & Schaefer, R. K. (2021). Night-Time Ionospheric Localized Enhancements (NILE) Observed in North America Following Geomagnetic Disturbances. *J Geophys Res Space Phys*, *126*(9), e2021JA029324. https://doi.org/10.1029/2021JA029324

Datta-Barua, S., Mannucci, A. J., Walter, T., & Enge, P. (2008). Altitudinal variation of midlatitude localized TEC enhancement from ground- and space-based measurements. *Space Weather, 6*(10), S10D06. https://doi.org/10.1029/2008sw000396

Fejer, B. G., & Scherliess, L. (1995). Time dependent response of equatorial ionospheric electric fields to magnetospheric disturbances. *Geophysical Research Letters*, *22*(7), 851-854. https://doi.org/10.1029/95gl00390

Finlay, C. C., Kloss, C., Olsen, N., Hammer, M. D., Toffner-Clausen, L., Grayver, A., & Kuvshinov, A. (2020). The CHAOS-7 geomagnetic field model and observed changes in the South Atlantic Anomaly. *Earth Planets Space*, *72*(1), 156. https://doi.org/10.1186/s40623-020-01252-9

Foster, J. C., & Rideout, W. (2007). Storm enhanced density: magnetic conjugacy effects. *Annales Geophysicae, 25*(8), 1791-1799. https://doi.org/10.5194/angeo-25-1791-2007

Foster, J. C., & Coster, A. J. (2007). Conjugate localized enhancement of total electron content at low latitudes in the American sector. *Journal of Atmospheric and Solar-Terrestrial Physics, 69*(10-11), 1241-1252. https://doi.org/10.1016/j.jastp.2006.09.012

Horvath, I., & Lovell, B. C. (2008). Formation and evolution of the ionospheric plasma density shoulder and its relationship to the superfountain effects investigated during the 6 November 2001 great storm. *Journal of Geophysical Research: Space Physics*, *113*(A12), A12315. https://doi.org/10.1029/2008ja013153

Huang, C. M. (2013). Disturbance dynamo electric fields in response to geomagnetic storms occurring at different universal times. *Journal of Geophysical Research: Space Physics*, *118*(1), 496-501. https://doi.org/10.1029/2012ja018118

Immel, T. J., & Mannucci, A. J. (2013). Ionospheric redistribution during geomagnetic storms. *Journal of Geophysical Research: Space Physics*, *118*(12), 7928-7939. https://doi.org/10.1002/2013JA018919

Kuai, J., Li, Q., Zhong, J., Zhou, X., Liu, L., Yoshikawa, A., Hu, L., Xie, H., Huang, C., Yu, X., Wan, X., & Cui, J. (2021). The Ionosphere at Middle and Low Latitudes Under Geomagnetic Quiet Time of December 2019. *Journal of Geophysical Research: Space Physics*, *126*(6), e2020JA028964. https://doi.org/10.1029/2020ja028964

Li, Q., Hao, Y., Zhang, D., & Xiao, Z. (2018). Nighttime Enhancements in the Midlatitude Ionosphere and Their Relation to the Plasmasphere. *Journal of Geophysical Research: Space Physics, 123*(9), 7686-7696. https://doi.org/10.1029/2018ja025422

Lockwood, M. (2023). Universal Time Effects on Substorm Growth Phases and Onsets. *Journal of Geophysical Research: Space Physics*, *128*(11), e2023JA031671. https://doi.org/10.1029/2023ja031671

Lockwood, M., Haines, C., Barnard, L. A., Owens, M. J., Scott, C. J., Chambodut, A., & McWilliams, K.

A. (2021). Semi-annual, annual and Universal Time variations in the magnetosphere and in geomagnetic activity: 4. Polar Cap motions and origins of the Universal Time effect. *Journal of Space Weather and Space Climate, 11*, 27. https://doi.org/10.1051/swsc/2020077

Lockwood, M., Owens, M. J., Barnard, L. A., Haines, C., Scott, C. J., McWilliams, K. A., & Coxon, J. C. (2020). Semi-annual, annual and Universal Time variations in the magnetosphere and in geomagnetic activity: 1. Geomagnetic data. *Journal of Space Weather and Space Climate, 10*, 23. https://doi.org/10.1051/swsc/2020023

Mannucci, A. J., Tsurutani, B. T., Iijima, B. A., Komjathy, A., Saito, A., Gonzalez, W. D., Guarnieri, F. L., Kozyra, J. U., & Skoug, R. (2005). Dayside global ionospheric response to the major interplanetary events of October 29–30, 2003 "Halloween Storms". *Geophysical Research Letters*, *32*(12), L12S02. https://doi.org/10.1029/2004gl021467

Maruyama, T., Ma, G., & Tsugawa, T. (2013). Storm-induced plasma stream in the low-latitude to midlatitude ionosphere. *Journal of Geophysical Research: Space Physics*, *118*(9), 5931-5941. https://doi.org/10.1002/jgra.50541

Obana, Y., Maruyama, N., Shinbori, A., Hashimoto, K. K., Fedrizzi, M., Nosé, M., Otsuka, Y., Nishitani, N., Hori, T., Kumamoto, A., Tsuchiya, F., Matsuda, S., Matsuoka, A., Kasahara, Y., Yoshikawa, A., Miyoshi, Y., & Shinohara, I. (2019). Response of the Ionosphere-Plasmasphere Coupling to the September 2017 Storm: What Erodes the Plasmasphere so Severely? *Space Weather, 17*(6), 861-876. https://doi.org/10.1029/2019sw002168

Østgaard, N., Vondrak, R. R., Gjerloev, J. W., & Germany, G. (2002). A relation between the energy deposition by electron precipitation and geomagnetic indices during substorms. *Journal of Geophysical Research: Space Physics, 107*(A9), 1246. https://doi.org/10.1029/2001ja002003

Park, J., Lühr, H., Jakowski, N., Gerzen, T., Kil, H., Jee, G., Xiong, C., Wook Min, K., & Noja, M. (2012). A long-lived band of plasma density enhancement at mid-latitudes during the 2003 Halloween magnetic storm. *Journal of Atmospheric and Solar-Terrestrial Physics*, *80*, 100-110. https://doi.org/10.1016/j.jastp.2012.03.009

Perlongo, N. J., & Ridley, A. J. (2016). Universal time effect in the response of the thermosphere to electric field changes. *Journal of Geophysical Research: Space Physics*, *121*(4), 3681-3698. https://doi.org/10.1002/2015ja021636

Pradipta, R., Valladares, C. E., & Doherty, P. H. (2015). An effective TEC data detrending method for the study of equatorial plasma bubbles and traveling ionospheric disturbances. *Journal of Geophysical Research: Space Physics*, *120*(12), 11,048–011,055. https://doi.org/10.1002/2015ja021723

Rajesh, P. K., Liu, J. Y., Balan, N., Lin, C. H., Sun, Y. Y., & Pulinets, S. A. (2016). Morphology of midlatitude electron density enhancement using total electron content measurements. *Journal of Geophysical Research: Space Physics, 121*(2), 1503-1517. https://doi.org/10.1002/2015ja022251

Russell, C. T., & McPherron, R. L. (1973). Semiannual variation of geomagnetic activity. *Journal of Geophysical Research*, *78*(1), 92-108. https://doi.org/10.1029/JA078i001p00092

Tsurutani, B., Mannucci, A., Iijima, B., Abdu, M. A., Sobral, J. H. A., Gonzalez, W., Guarnieri, F., Tsuda, T., Saito, A., Yumoto, K., Fejer, B., Fuller-Rowell, T. J., Kozyra, J., Foster, J. C., Coster, A., & Vasyliunas, V. M. (2004). Global dayside ionospheric uplift and enhancement associated with interplanetary electric fields. *Journal of Geophysical Research: Space Physics, 109*(A8), A08302. https://doi.org/10.1029/2003ja010342

Wan, X., Zhong, J., Xiong, C., Wang, H., Liu, Y., Li, Q., Kuai, J., Weng, L., & Cui, J. (2021). Persistent

Occurrence of Strip-Like Plasma Density Bulges at Conjugate Lower-Mid Latitudes During the September 8-9, 2017 Geomagnetic Storm. *Journal of Geophysical Research: Space Physics*, *126*(5), e2020JA029020. https://doi.org/10.1029/2020ja029020

Wan, X., Zhong, J., Zhang, S. R., Xiong, C., Wang, H., Liu, Y., Huang, F., Li, Q., Kuai, J., Chen, J., & Hao, Y. (2022). Disturbance Neutral Winds Effects on the Ionospheric Strip-Like Bulge at Lower-Middle Latitudes. *Journal of Geophysical Research: Space Physics*, *127*(8), e2022JA030541. https://doi.org/10.1029/2022ja030541

Wang, H., Zhang, K. D., Wan, X., & Lühr, H. (2017). Universal time variation of high-latitude thermospheric disturbance wind in response to a substorm. *Journal of Geophysical Research: Space Physics*, *122*(4), 4638-4653. https://doi.org/10.1002/2016ja023630

Xiong, C., Lühr, H., Sun, L., Luo, W., Park, J., & Hong, Y. (2019). Long-Lasting Latitudinal Four-Peak Structure in the Nighttime Ionosphere Observed by the Swarm Constellation. *Journal of Geophysical Research: Space Physics*, *124*(11), 9335-9347. https://doi.org/10.1029/2019ja027096

Zhang, H., Cai, H. T., Wan, X., Hu, K., Xiong, C., Gao, S. Z., & Yang, L. B. (2024). The Altitudinal Dependences of the Inter-Hemispheric Asymmetry in the Mid-Latitude Ionospheric Post-Midnight Enhancement During Equinox. *Journal of Geophysical Research: Space Physics*, *129*(1), e2023JA032260. https://doi.org/10.1029/2023ja032260

Zhang, X. X., He, F., Lin, R. L., Fok, M. C., Katus, R. M., Liemohn, M. W., Gallagher, D. L., & Nakano, S. (2017). A new solar wind-driven global dynamic plasmapause model: 1. Database and statistics. *Journal of Geophysical Research: Space Physics*, *122*(7), 7153-7171. https://doi.org/10.1002/2017ja023912

Zhong, J., Lei, J., Yue, X., Luan, X., & Dou, X. (2019). Middle-Latitudinal Band Structure Observed in the Nighttime Ionosphere. *Journal of Geophysical Research: Space Physics*, *124*(7), 5857-5873. https://doi.org/10.1029/2018ja026059